

# Learning to Quantize and Precode in Massive MIMO Systems for Energy Reduction: a Graph Neural Network Approach

Thomas Feys, Liesbet Van der Perre, François Rottenberg

**Abstract**—Massive MIMO systems are moving toward increased numbers of radio frequency chains, higher carrier frequencies and larger bandwidths. As such, digital-to-analog converters (DACs) are becoming a bottleneck in terms of hardware complexity and power consumption. In this work, non-linear precoding for coarsely quantized downlink massive MIMO is studied. Given the NP-hard nature of this problem, a graph neural network (GNN) is proposed that directly outputs the precoded quantized vector based on the channel matrix and the intended transmit symbols. The model is trained in a self-supervised manner, by directly maximizing the achievable rate. To overcome the non-differentiability of the objective function, introduced due to the non-differentiable DAC functions, a straight-through Gumbel-softmax estimation of the gradient is proposed. The proposed method achieves a significant increase in achievable sum rate under coarse quantization. For instance, in the single-user case, the proposed method can achieve the same sum rate as maximum ratio transmission (MRT) by using one-bit DACs as compared to 3 bits for MRT. This reduces the DAC's power consumption by a factor 4-7 and 3 for baseband and RF DACs respectively. This, however, comes at the cost of increased digital signal processing power consumption. When accounting for this, the reduction in overall power consumption holds for a system bandwidth up to 3.5 MHz for baseband DACs, while the RF DACs can maintain a power reduction of 2.9 for higher bandwidths. Notably, indirect effects, which further reduce the power consumption, such as a reduced fronthaul consumption and reductions in other components, are not considered in this analysis.

**Index Terms**—MIMO systems, neural networks, digital-to-analog converter, nonlinear distortion.

## I. INTRODUCTION

### A. Problem Statement

Massive multiple input multiple output (MIMO) is a key enabler for 5G and is expected to be further developed for the next generation [1]. Massive MIMO leverages many antennas at the base station (BS) to spatially focus the signal to the user locations. This increases the achievable data rates and the spectral efficiency [2]. While the capacity is increased, this does incur a significant hardware cost. In a fully digital massive MIMO system, each radio frequency chain is typically equipped with its own, analog-to-digital converter (ADC), DAC, power amplifier (PA) and antenna, among others.

The use of many radio frequency chains increases both the hardware complexity and the power consumption. To combat this, in this work we focus on reducing the bit-width of DACs. This is motivated by the current move towards higher carrier frequencies and higher bandwidths [3], which further increases

the complexity and the power consumption of the DACs. The reason for this increased power consumption is threefold. First, the power consumption of typical current steering DACs scales exponentially with the number of bits and linearly with the sampling frequency [4]. This raises concerns given the ever-increasing bandwidth of wireless systems. Second, radio frequency digital-to-analog converters (RF-DACs) are becoming increasingly popular in wireless systems due to their ability to directly synthesize the radio frequency (RF) signal at the desired carrier frequency, which reduces analog complexity [5]. This is possible by relying on a high oversampling factor to place the signal at the desired carrier frequency, bypassing traditional analog upconversion. However, due to the increased oversampling factor, coupled with the current move towards higher carrier frequencies and higher bandwidths, the power consumption of these RF-DACs is significantly higher as compared to traditional DACs. To offset this increased power consumption, we investigate how the bit-width can be reduced, providing reduced power consumption in the DACs, while maintaining system performance. Finally, the spurious free dynamic range, that is the frequency range over which the DAC operates free from unwanted spurious signals, is limited by the resolution of the DAC [6]. Hence, high resolution DACs become problematic at higher carrier frequencies and bandwidths, as additional nonlinearities are introduced. Next to this, decreasing the bit-width can have significant indirect benefits. For instance, the power consumption of the digital fronthaul, which connects the baseband unit with the antenna array, can be significantly reduced when fewer bits are considered. Alternatively, if the bit-width reduction can be propagated into the baseband processing this would have a big impact on its power consumption.

Consequently, low-resolution DACs are vital to overcome these hardware limitations and reduce the power consumed in the many DACs. However, by using lower resolution DACs a significant quantization error is introduced, which limits the signal-to-distortion ratio (SDR) and the achievable data rates. To overcome this, we present an approach to limit this quantization distortion by leveraging the degrees of freedom available from the many antennas at the BS. This is done by proposing a neural network (NN)-based non-linear precoding scheme that mitigates this distortion. By doing so, the DACs can utilize fewer bits, while a high achievable data rate can be maintained in the network.

### B. State-of-the-Art Quantization in Massive MIMO

Quantization in Massive MIMO systems has been widely studied. A rich body of literature focuses on the effects of ADCs at the receiver [7]–[11]. In this work, we focus on the effects of DAC distortion. Two trends have emerged when dealing with DAC distortion in MIMO systems. On the one hand, there is a focus on 1-bit systems, largely driven by their analytical tractability and simplified hardware design. On the other hand, several works tackle the more general few-bit case.

The authors are with ESAT-DRAMCO, Campus Ghent, KU Leuven, Belgium (email: thomas.feys@kuleuven.be).

We thank NVIDIA for providing the GPU that accelerated our simulations. Partially funded by 6GTandem part of SNS JU under the European Union's Horizon Europe research and innovation program, Grant 101096302.

This work is Co-funded by the European Union under Grant Agreement 101191936. Views and opinions expressed are however those of the author(s) only and do not necessarily reflect those of all 6GTandem/SUSTAIN-6G consortium parties nor those of the European Union or the SNS-JU (granting authority). Neither the European Union nor the granting authority can be held responsible for them.

However, due to the intractability, simplifying assumptions have been made which are only valid when many users or many bits are considered. As shown in this work, distortion due to the DACs is most limiting when few users are present. This is because distortion becomes more spatially spread out as the number of users rises, similar to the case of non-linear PA distortion [12]. Hence, there is a need for a solution to the quantization-aware precoding problem for the case of few users and few bits.

1) *1-bit DACs*: In [13], a 1-bit quantized zero forcing (ZF) precoder is studied. It is shown that when the number of transmit antennas goes to infinity, the received signals are scaled versions of the desired symbols. Next to this, in [14] a two-stage digital-analog precoder is proposed that takes into account one-bit DACs at the transmitter and one-bit ADC at the receiver. Additionally, in [15], [16] several one-bit non-linear precoders are proposed i) based on a semidefinite relaxation leading to a convex problem, ii) based on a squared  $l_\infty$ -norm relaxation which also leads to a convex problem and iii) based on sphere decoding rather than solving the non-linear quantized precoding problem, which essentially is an NP-hard closest-vector problem, through exhaustive search.

2) *Few-bit DACs*: In [17], minimum mean squared error (MMSE) linear processing is proposed where 4-6 bit DACs are deployed at the BS. However, this work relies on the high-resolution assumption to specify the quantization error, i.e., when the number of bits  $b$  is large, the quantization error of an optimal non-uniform quantizer approximately scales with  $2^{-2b}$ . The work in [18] optimizes the energy efficiency while taking into account the power consumption and distortion due to low-resolution ADCs and DACs. However, the distortion covariance matrix is assumed to be diagonal (i.e., uncorrelated distortion). This assumption holds when many users with an independently and identically distributed (i.i.d.) Rayleigh fading channel are considered [19]. Hence, this assumption does not hold in the most critical case for quantization distortion, i.e., the few user-case. Similarly, in [20] the quantized single-user MIMO case is studied. The energy efficiency of digital and hybrid precoders is evaluated. However, this study also relies on the assumption of uncorrelated distortion, which only holds when many users are present.

In summary, there is a need for transmit processing that addresses the case of few-bit DACs when few users are present. In this study, we overcome this gap by proposing neural network-based non-linear precoders that are trained for both the one-bit and few-bit DAC cases, without relying on assumptions that only hold for high-resolution DACs or a high number of users.

### C. State-of-the-Art Neural Network-based Precoding

NNs have become an interesting approach for learning to precode. Some works focus on learning NN-based precoders as a low-complexity alternative to high-complexity conventional precoding algorithms [21]–[23]. Furthermore, NN-based precoding has been used to solve precoding problems that do not have a simple solution and where conventional algorithms show limited performance [22], [24], [25]. In these works a wide range of NN architectures is used ranging from multilayer perceptrons (MLPs), convolutional neural networks (CNNs), transformers and GNNs. Each of these architectures has a certain structure that limits the types of functions these NNs can learn. In general, the aim of selecting a certain architecture is to reduce the hypothesis space of the NN,

that is the space of all possible functions the NN can learn. Reducing the hypothesis space typically corresponds to a NN that has fewer trainable parameters. Consequently, less training data is needed and training becomes easier. However, the cost of reducing the hypothesis space is a less expressive model, which can cause the NN to not be able to learn the desired function. However, if one can reduce the hypothesis space in an informed manner such that the desired function is still covered by this reduced hypothesis space, the reduced expressivity of the model does not affect the learning performance [24], [26]. Note that this is closely linked to the bias-variance trade-off [27]. A model with a large hypothesis space will have a low bias but high variance, while reducing the hypothesis space leads to lower variance, but might increase the bias. The goal is to find a hypothesis space with an optimal trade-off such that both the bias and variance are minimized. Recent works have shown that, for linear precoding, GNNs are especially well-suited [24], [28], [29]. This is due to their permutation equivariance properties. Simply put, if the order of the rows/columns in the input matrix to the NN is permuted, the order of the rows/columns in the output matrix should be permuted accordingly. Concerning the linear precoding problem, if the rows/columns of the channel matrix (input) are permuted, the rows/columns of the precoding matrix (output) should be permuted accordingly. This is an inherent property of linear precoders, which is respected by using GNNs. Hence, by using GNNs the hypothesis space is reduced to only include permutation equivariant functions, thereby reducing the variance while keeping the bias low.

Concerning quantization-aware precoding, several works have introduced the use of NNs for the 1-bit case. In [30], the authors propose to unfold the biconvex 1-bit precoding algorithm from [31]. Next to this, in [32] non-linear precoding for the 1-bit case is learned in a supervised manner.

More broadly, the quantized precoding problem can be seen as a combinatorial problem, as the goal is to select the best output level at each DAC from a finite set. Our work is inspired by a sub-field of deep learning, known as neural combinatorial optimization (NCO) [33]–[35]. NCO aims at training NNs that can solve combinatorial problems. Given the NP-hard nature of many combinatorial problems, it is often hard to obtain optimal solutions that can be used as labels. Hence, supervised learning for combinatorial optimization is often costly or impossible. Consequently, NCO is typically done in combination with reinforcement learning, where the proposed solution by the NN is evaluated. This evaluation is then used as a reward signal to update the weights of the NN [33]. More recently, one-shot neural combinatorial solvers have been introduced that do not rely on reinforcement learning [36]. These methods directly predict the decision variables for the problem. The decision variables are then evaluated using a differentiable objective function. This differentiable objective function is then used as a self-supervised loss function, to update the weights of the NN through stochastic gradient descent [36]. The benefit of this methodology is *i)* that no labels are required, *ii)* unsupervised learning typically generalizes better as compared to the mimic learning that happens in the supervised setting, which can be attributed to the unsupervised loss function capturing more underlying physical insights of the problem, and *iii)* it is empirically more efficient than reinforcement learning [36]. The main drawback of this method is that the objective function should be differentiable, which is not always the case. In this work, we follow the one-shot neural combinatorial solver methodology. Given the non-differentiable nature of

our objective function (caused by the non-differentiable DAC functions), we utilize a Gumbel-softmax-based [37] relaxation which renders the objective function differentiable in the backward pass but still discrete in the forward pass.

#### D. Contributions

In this work, a novel GNN-based non-linear precoding method is proposed that achieves high data rates under coarse quantization in a downlink massive MIMO system. Section II outlines the system model. In Section III the critical case in terms of distortion is identified as the few users, few bits case. Hence, the proposed precoder is developed considering few users and few bits, i.e., it does not rely on assumptions of uncorrelated distortion that are only valid when many users are present or many bits are considered, as is often done in the current literature. In Section IV, based on the permutation equivariance properties of the non-linear precoding problem a GNN is proposed that captures these properties. Additionally, an unsupervised training procedure is outlined to train this GNN. This is especially challenging given the non-differentiable nature of the objective function, caused by the non-differentiable DAC functions. To overcome this we propose a Gumbel-softmax-based relaxation of the objective function. In Section V the complexity of the proposed GNN is computed. Section VI provides extensive simulation results to validate the performance of the proposed GNN. It is shown that the proposed precoder can achieve a significant increase in terms of achievable sum rate. Radiation patterns illustrate that this gain is achieved by transmitting the distortion in non-user directions. In Section VII the reduction in power consumption of the DACs is computed while taking into account the additional processing power consumption of the GNN. When solely considering the DACs consumption, it is shown that the proposed method reduces the power consumption by a factor of 4-7. However, when taking the GNN processing power consumption into account the power reduction is only achieved for bandwidths up to 3.5 MHz, without taking into account indirect effects such as reduced fronthaul consumption. Finally, Section IX concludes the paper.

#### Notations

Vectors and matrices are denoted by bold lowercase and bold uppercase letters respectively. A vector function is denoted by a bold letter while a scalar function is denoted by a non-bold letter. Superscripts  $(\cdot)^*$ ,  $(\cdot)^\top$  and  $(\cdot)^H$  stand for the conjugate, transpose and Hermitian transpose operators respectively. The expectation is  $\mathbb{E}(\cdot)$ . The  $M \times M$  identity matrix is given by  $\mathbf{I}_M$ . The main diagonal of a square matrix  $\mathbf{A}$  is given by  $\text{diag}(\mathbf{A})$ . The trace of a matrix is given by  $\text{Tr}(\cdot)$ . The element at location  $(i, j)$  in matrix  $\mathbf{A}$  is indicated as  $[\mathbf{A}]_{i,j}$ . Similarly, element  $i$  of vector  $\mathbf{a}$  is denoted as  $[\mathbf{a}]_i$  or in scalar form as  $a_i$ .  $\mathcal{G} = (\mathcal{V}, \mathcal{E})$  denotes a graph where  $\mathcal{V}$  is the set of nodes and  $\mathcal{E}$  the set of edges. The edge going from node  $a \in \mathcal{V}$  to node  $b \in \mathcal{V}$  is denoted as  $(a, b) \in \mathcal{E}$ . The neighborhood of a node  $a$  is denoted as  $\mathcal{N}(a) = \{b \in \mathcal{V} : (a, b) \in \mathcal{E}\}$ . The indicator function denotes one-hot encoded vectors where  $\mathbb{1}_i^N$  is a length  $N$  vector containing zeros except for a one at index  $i$ .

## II. SYSTEM MODEL

### A. Linear Quantized Precoding

Consider a BS with  $M$  transmit antennas and  $K$  single antenna users, operating in the downlink. When considering

digital full-precision linear precoding, the precoded vector is obtained as  $\mathbf{x} = \mathbf{W}\mathbf{s}$ , where  $\mathbf{x} \in \mathbb{C}^M$  are the precoded symbols,  $\mathbf{W} \in \mathbb{C}^{M \times K}$  is the precoding matrix and  $\mathbf{s} \in \mathbb{C}^K$  is the symbol vector, where the symbols between different users are uncorrelated and zero mean. When a single user is present we consider MRT precoding, with precoding matrix  $\mathbf{W}^{\text{MRT}} = \alpha_{\text{norm}} \mathbf{H}^*$ . When multiple users are present ZF precoding is considered as  $\mathbf{W}^{\text{ZF}} = \alpha_{\text{norm}} \mathbf{H}^* (\mathbf{H}^\top \mathbf{H}^*)^{-1}$ . Both for MRT and ZF precoding the power normalization constant is defined as  $\alpha_{\text{norm}} = \sqrt{P_T / \text{Tr}(\mathbf{W}\mathbf{W}^H)}$  so that the total transmit power is normalized to  $P_T$ . After precoding, the digital baseband signal  $\mathbf{x}$  is quantized. This is done for the real and imaginary dimensions per antenna

$$\mathbf{y} = \mathcal{Q}(\mathbf{x}) = [\mathcal{Q}(\Re\{x_0\}) + j\mathcal{Q}(\Im\{x_0\}), \dots, \mathcal{Q}(\Re\{x_{M-1}\}) + j\mathcal{Q}(\Im\{x_{M-1}\})]^\top \quad (1)$$

where  $\mathcal{Q}(\cdot) : \mathbb{C}^M \mapsto \mathbb{C}^M$  denotes the quantization function which characterizes the combined operation of the  $2M$  DACs at the BS and  $\mathcal{Q}(\cdot) : \mathbb{R} \mapsto \mathcal{L}$  denotes the real-valued quantizer. These quantizers are further detailed in Section II-B.

This quantization can be characterized by the additive quantization noise model (AQNM), originally proposed by [38], which is a special case of the Bussgang decomposition with the nonlinear function being a quantizer that represents each quantization interval by its mean value [39]. In this work, we follow the convention of the Bussgang decomposition

$$\mathbf{y} = \mathcal{Q}(\mathbf{x}) = \Phi_\alpha \mathbf{x} + \mathbf{q} \quad (2)$$

where the distortion  $\mathbf{q}$  is uncorrelated with  $\mathbf{x}$ , i.e.,  $\mathbb{E}(\mathbf{x}\mathbf{q}^H) = \mathbf{0}$ . The Bussgang matrix is given by  $\Phi_\alpha = \text{diag}(\alpha_0, \dots, \alpha_{M-1}) \in \mathbb{R}^{M \times M}$ , where  $\alpha_m = \frac{\mathbb{E}(y_m x_m^*)}{\mathbb{E}(|x_m|^2)}$ . The link with the AQNM can be made by defining the normalized mean squared quantization error (NMSQE) after the  $m^{\text{th}}$  DAC as

$$\beta_m = \frac{\mathbb{E}((x_m - y_m)(x_m - y_m)^*)}{\mathbb{E}(|x_m|^2)} \quad (3)$$

and relating the Bussgang gain to the NMSQE after each DAC as  $\Phi_\alpha = \mathbf{I}_M - \Phi_\beta$ , where  $\Phi_\beta = \text{diag}(\beta_0, \dots, \beta_{M-1}) \in \mathbb{R}^{M \times M}$ .

### B. Quantization

1) *Quantization of a Complex-Valued Vector:* The precoded (unquantized) vector is given by  $\mathbf{x} \in \mathbb{C}^M$ . After quantization, the precoded vector is given by  $\mathbf{y} \in \mathcal{C}^M$ , where the set  $\mathcal{C}$  is the set of complex output levels/codebook. When considering infinite precision the set  $\mathcal{C}$  coincides with  $\mathbb{C}$ . However, due to the use of DACs, the set  $\mathcal{C}$  has a finite cardinality. The set of real-valued DAC outputs is given by  $\mathcal{L} = \{l_0, \dots, l_{L-1}\} \subset \mathbb{R}$ , where  $l_i$  are the output values/levels and  $L = |\mathcal{L}| = 2^b$  is the number of quantization levels with  $b$  the number of considered bits per real dimension. For each BS antenna the same output set is considered for the real and imaginary parts. The set of complex-valued DAC outputs is then given by  $\mathcal{C} = \mathcal{L} \times \mathcal{L}$ . This can be seen as applying one real-valued DAC to the real part of the precoded symbol at each antenna and one real-valued DAC to the imaginary part. The real-valued quantizer partitions the real line  $\mathbb{R}$  into  $L$  cells  $\mathcal{R}_i$  for  $i = 0, 1, \dots, L-1$ . The  $i$ th cell is defined as  $\mathcal{R}_i = \{x \in \mathbb{R} : \mathcal{Q}(x) = l_i\}$  [40]. From this definition, it follows that  $\bigcup_i \mathcal{R}_i = \mathbb{R}$  and  $\mathcal{R}_i \cap \mathcal{R}_j = \emptyset$ . Additionally, each cell is fully described by its boundary points/thresholds

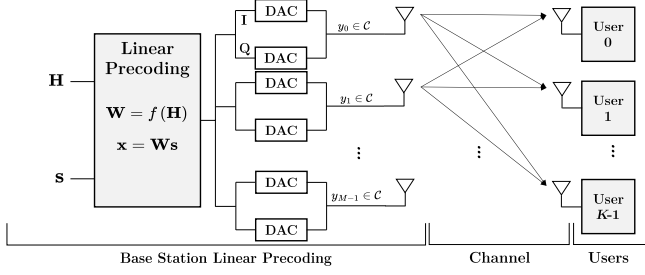


Fig. 1: Simplified system overview of linear quantized precoding.

$\mathcal{T} = \tau_0, \dots, \tau_L$ ,  $\mathcal{R}_i = (\tau_i, \tau_{i+1}]$  for  $i = 0, \dots, L-1$  [40]. For quantizers operating on unbounded inputs typically  $\tau_0 = -\infty$  and  $\tau_L = +\infty$ . The optimal values of the output labels and thresholds depend on the type of quantization used and the input distribution, as described in the next section.

2) *Non-Uniform Quantization*: The input distribution in this work is Gaussian, which is a valid assumption for orthogonal frequency division multiplexing (OFDM) systems [41]. For a real-valued Gaussian input, uniform quantization is not optimal in the minimum mean squared quantization error (MMSQE) sense [40]. A MMSQE non-uniform quantizer can be found by solving  $\min_{\mathcal{L}, \mathcal{T}} \mathbb{E}((x - \mathcal{Q}(x))^2) = \sum_{i=1}^N \int_{\mathcal{R}_i} (x - l_i)^2 f_X(x) dx$ . The Max-Lloyd algorithm as described in [40], [42] can be used to find the optimal output levels and thresholds. This is a hill-climbing algorithm, which can lead to local optima in the solution, hence it is advised to run the algorithm for several initialization points. This is done to obtain the output levels and thresholds used in this work.

3) *Input Normalization*: To achieve optimal quantization the input distribution to the DAC should be  $\mathcal{CN}(0, 1)$ . The transmit symbols are  $s_k \sim \mathcal{CN}(0, 1)$ . However, the input to the DAC is not the transmit symbol but the precoded symbol  $x_m = \sum_k w_{m,k} s_k = \mathbf{w}_m^T \mathbf{s}$ . As such, the precoded symbol is a scaled random variable that is complex normal distributed. Its power (variance) can be computed as  $\mathbb{E}(|x_m|^2) = \|\mathbf{w}_m\|_2^2$ . To adjust the power of the input signal (per antenna chain) to the dynamic range of the DAC, an input normalization<sup>1</sup> scales the input as  $\tilde{x}_m = \frac{1}{\sqrt{\rho_m}} x_m$ , where  $\rho_m$  is a scalar normalization factor. If  $\rho_m = \|\mathbf{w}_m\|_2^2$  the signal power is rescaled to one. This normalized signal is sent to the DAC to be quantized as  $\tilde{y}_m = \mathcal{Q}(\tilde{x}_m)$ . After quantizing this normalized signal, the output of the DAC should be denormalized as  $y_m = \sqrt{\rho_m} \tilde{y}_m$ . This denormalization can be taken into account by the amplification stage, while the normalization can be performed in the digital signal processing.

### C. Non-Linear Neural Network-based Quantized Precoding

NN-based non-linear precoding is considered. This entails that a NN is used to learn a mapping from the channel matrix and symbol vector to the precoded quantized symbol vector. The function we want to learn can be represented as

$$\mathbf{y}_{\text{NL}} = f(\mathbf{H}, \mathbf{s}; \boldsymbol{\theta}) \quad (4)$$

where  $f(\cdot, \cdot) : \mathbb{C}^{M \times K} \times \mathbb{C}^K \mapsto \mathbb{C}^M$  represents the NN, i.e., a learned non-linear function mapping parametrized by its

<sup>1</sup>This is similar to the automatic gain control typically applied at the receiver before the ADC.

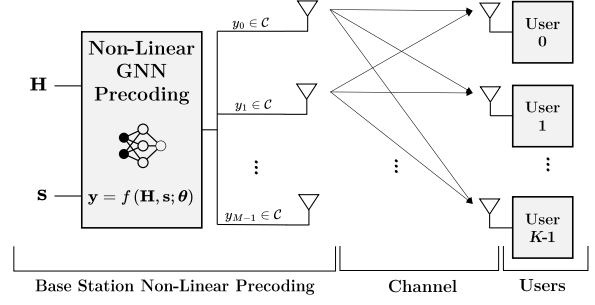


Fig. 2: Simplified system overview of non-linear quantized precoding.

trainable weights  $\boldsymbol{\theta}$ . Given that there is no explicit quantization step for non-linear precoding, the Bussgang decomposition with respect to  $\mathbf{x}$  can no longer be computed. More generally, we define the Bussgang decomposition between the precoded quantized signal  $\mathbf{y}$  and the intended transmit symbols  $\mathbf{s}$  as

$$\mathbf{y} = \mathbf{G}\mathbf{s} + \mathbf{q} \quad (5)$$

where the Bussgang gain matrix is no longer a square diagonal matrix, it is now defined as  $\mathbf{G} = \mathbb{E}(\mathbf{y}\mathbf{s}^H) (\mathbb{E}(\mathbf{s}\mathbf{s}^H))^{-1} = \mathbb{E}(\mathbf{y}\mathbf{s}^H)$ . The link with the Bussgang decomposition under linear precoding in (2) is easily made using  $\mathbf{x} = \mathbf{W}\mathbf{s}$ , as  $\mathbf{G} = \boldsymbol{\Phi}_\alpha \mathbf{W}$ .

### D. Achievable Sum Rate

Regardless of which precoding technique is considered, the received signal can be written as

$$\mathbf{r} = \mathbf{H}^T \mathbf{y} + \mathbf{v} \quad (6)$$

where  $\mathbf{r} \in \mathbb{C}^K$  is the received signal vector,  $\mathbf{H} \in \mathbb{C}^{M \times K}$  the channel matrix,  $\mathbf{y} \in \mathbb{C}^M$  the precoded and quantized transmit symbols and  $\mathbf{v} \in \mathbb{C}^K$  additive white Gaussian noise with covariance matrix  $\sigma_v^2 \mathbf{I}_K$ . Using (5), the received signal for user  $k$  can be written as

$$r_k = \underbrace{\mathbf{h}_k^T \mathbf{g}_k s_k}_{\text{intended signal}} + \underbrace{\sum_{k' \neq k} \mathbf{h}_k^T \mathbf{g}_{k'} s_{k'}}_{\text{user interference}} + \underbrace{\mathbf{h}_k^T \mathbf{q}}_{\text{distortion}} + \underbrace{v_k}_{\text{noise}}. \quad (7)$$

Hence the signal-to-noise-and-interference-and-distortion ratio (SNIDR) for user  $k$  can be written as

$$\text{SNIDR}_k = \frac{|\mathbf{h}_k^T \mathbf{g}_k|^2}{\sum_{k' \neq k} |\mathbf{h}_k^T \mathbf{g}_{k'}|^2 + \mathbf{h}_k^T \mathbb{E}(\mathbf{q}\mathbf{q}^H) \mathbf{h}_k^* + \sigma_v^2}. \quad (8)$$

An achievable sum rate  $R_{\text{sum}}$ , i.e., a lower bound on the capacity, can be obtained by considering a worst-case scenario, where the noise and quantization distortion are jointly Gaussian distributed and independent from the data symbols

$$R_{\text{sum}} = \sum_{k=0}^{K-1} \log_2(1 + \text{SNIDR}_k). \quad (9)$$

### E. Radiation Patterns

In Sections III and VI a number of radiation patterns are evaluated. For this, a pure line-of-sight (LOS) channel

$\mathbf{h}_{\text{los}}(\phi_k)$  is considered, the channel coefficient from antenna  $m$  to user  $k$  is

$$h_{m,k} = e^{-jm \frac{2\pi}{\lambda_c} d \cos(\phi_k)}. \quad (10)$$

Here  $m \frac{2\pi}{\lambda_c} d \cos(\phi_k)$  is the antenna-dependent phase shift when considering a uniform linear array (ULA) and a narrowband system,  $\lambda_c$  is the carrier frequency,  $d = \lambda_c/2$  the antenna spacing and  $\phi_k$  the user angle. The radiation pattern of the intended signal in an arbitrary direction  $\tilde{\phi}$  can be written as

$$P_{\text{lin}}(\tilde{\phi}) = \mathbb{E} \left( |\mathbf{h}_{\text{los}}^{\text{T}}(\tilde{\phi}) \mathbf{G} \mathbf{s}|^2 \right) = \mathbf{h}_{\text{los}}^{\text{T}}(\tilde{\phi}) \mathbf{G} \mathbf{G}^H \mathbf{h}_{\text{los}}^*(\tilde{\phi}). \quad (11)$$

The radiation pattern of the quantization distortion is given by

$$P_{\text{dist}}(\tilde{\phi}) = \mathbb{E} \left( |\mathbf{h}_{\text{los}}^{\text{T}}(\tilde{\phi}) \mathbf{q}|^2 \right) = \mathbf{h}_{\text{los}}^{\text{T}}(\tilde{\phi}) \mathbb{E} (\mathbf{q} \mathbf{q}^H) \mathbf{h}_{\text{los}}^*(\tilde{\phi}). \quad (12)$$

The SDR radiation pattern is defined as  $P_{\text{SDR}}(\tilde{\phi}) = \frac{P_{\text{lin}}(\tilde{\phi})}{P_{\text{dist}}(\tilde{\phi})}$ .

### III. SPATIAL CHARACTERISTICS OF QUANTIZATION-INDUCED DISTORTION

When considering linear precoding techniques such as MRT and ZF, followed by a quantization step, the radiation patterns of both the linear and distortion signals can be characterized according to (11) and (12). In this section, these numerically obtained radiation patterns are analyzed in order to identify scenarios where the quantization distortion is most critical.

In Fig. 3 the radiation pattern of the distortion, the intended signal and SDR are depicted for  $K = 1$ ,  $b = 1$  and  $M = 32$ . For some pathological cases (for instance  $\phi \in \{0^\circ, 60^\circ, 90^\circ, 120^\circ, 180^\circ\}$ ), the beamforming gain assigned to the intended and distortion signal are identical, which leads to an SDR that is uniformly distributed in space, as seen in Fig. 3a. In most other cases, the distortion receives a beamforming gain in multiple directions, with the user direction being the dominant one, as seen in Fig. 3b. This leads to a small SDR in the user direction. Increasing the number of bits generally leads to identical but scaled radiation patterns, where the intended signal increases, the distortion decreases and the SDR increases.

In Fig. 4 the radiation pattern of the distortion, the intended signal and SDR are depicted for the multi-user case. In Fig. 4a two users are present, in this case, the distortion is radiated in a number of directions, with the two user directions being the most dominant ones. When the number of users increases to six in Fig. 4b the distortion is nearly uniformly distributed, hence receiving little to no beamforming gain. From these figures, it is clear that the distortion radiation pattern is more spatially spread out the more users are present. This is similar to the case of non-linear PA distortion [12]. Given this spatially spread out distortion, the SDR radiation pattern shows a clear peak in the user directions. Hence the more users are present, the less they are affected by distortion. Note that this discussion purely focuses on the distortion, while the low resolution of DACs can also lead to additional inter-user interference given that the low resolution leads to poorer interference cancellation. Nevertheless, when purely focusing on the distortion the most critical case arises when few users are present.

### IV. NEURAL NETWORKS FOR PRECODING

In this work, we consider NN-based non-linear precoding as described by (4). In this section, the training procedure is outlined, followed by the NN architecture that is selected.

#### A. General Training Procedure

The optimization problem we aim to solve in order to perform quantized non-linear precoding can be formulated as

$$\max_{\mathbf{y}_{\text{NL}} \in \mathcal{C}^M} R_{\text{sum}}(\mathbf{y}_{\text{NL}}) \quad \text{s.t.} \quad \mathbb{E}(\|\mathbf{y}_{\text{NL}}\|_2^2) \leq P_T \quad (13)$$

where the sum rate is computed according to (9). During training, the NN outputs a quantized precoded vector  $\mathbf{y}_{\text{NL}}$ . This precoded quantized vector can be used to compute the loss function, which is the sum rate according to (9)

$$\theta^* = \arg \min_{\theta} -R_{\text{sum}}(f(\mathbf{H}, \mathbf{s}; \theta)). \quad (14)$$

Given that the value of this sum rate directly depends on the output of the NN (i.e., the precoded quantized vector), the gradients of this loss function, with respect to the weights of the NN  $\theta$  can directly be computed using backpropagation. Given these gradients, the parameters of the NN are updated using the Adam optimizer [43]. Note that during training, for each channel realization, the NN is run  $N_s$  times, i.e., for  $N_s$  different symbols. The average power is then normalized to  $P_T$  by taking the expectation over these  $N_s$  symbols according to

$$\alpha = \frac{\sqrt{P_T}}{\mathbb{E}(\|\mathbf{y}_{\text{NL}}\|_2^2)}, \quad \mathbf{y}_{\text{norm}} = \alpha \mathbf{y}_{\text{NL}}. \quad (15)$$

Given the discrete nature of quantization, obtaining a gradient (or estimate thereof) of the loss function with respect to the weights of the NN is non-trivial. In the next subsection, the link between quantized precoding and classification is made, followed by a method to obtain a gradient estimate, which can be used to train the NN in an unsupervised manner.

#### B. Unsupervised Learning of Non-Linear Precoding

Given the discrete nature of the quantized precoding problem, the selection of the appropriate output levels can be seen as a classification problem per antenna, where the appropriate output levels need to be selected. However, the optimal output levels are unknown, hence there are no labels available to train the NN in a supervised manner.

1) *Intermediate Probability Mapping*: As a solution, let's consider unsupervised learning of non-linear precoding. For this, the NN uses an intermediate mapping to probability vectors, rather than producing the correct output levels directly. The output of the NN represents a probability vector per real and imaginary part of each antenna

$$\mathbf{p} = f(\mathbf{H}, \mathbf{s}; \theta), \quad \text{with} \quad \mathbf{p} \mid \mathbf{H}, \mathbf{s} \quad (16)$$

$$= [\mathbf{p}_{\Re,0}, \mathbf{p}_{\Im,0}, \dots, \mathbf{p}_{\Re,M-1}, \mathbf{p}_{\Im,M-1}]^{\text{T}} \quad (17)$$

where the intermediate mapping is  $f(\cdot, \cdot) : \mathbb{C}^{M \times K} \times \mathbb{C}^K \mapsto [0, 1]^{2M|\mathcal{L}|}$  and  $\mathbf{p} \in [0, 1]^{2M|\mathcal{L}|}$  represents the concatenation of the probability vectors for the real and imaginary parts of each antenna, where  $\mathbf{p}_{\Re,m}, \mathbf{p}_{\Im,m} \in [0, 1]^{|\mathcal{L}|}$  represent the probability vectors for the real and imaginary parts of the DAC output at antenna  $m$ . These probability vectors are conditioned on the channel matrix and symbol vector. However, this conditioning is often omitted for notational convenience. At inference time, the true output levels of DAC  $m$  can be found as the output levels  $l_i, l_j \in \mathcal{L}$  that are assigned the highest probability value. This gives  $y_m = l_i + l_j j$ , with

$$i = \arg \max_{i \in \{0, \dots, L-1\}} \mathbf{p}_{\Re,m}, \quad j = \arg \max_{j \in \{0, \dots, L-1\}} \mathbf{p}_{\Im,m}. \quad (18)$$



Fig. 3: Radiation pattern of the intended signal  $P_{\text{lin}}(\tilde{\phi})$ , distortion signal  $P_{\text{dist}}(\tilde{\phi})$  and SDR  $P_{\text{SDR}}(\tilde{\phi})$  in [dB] for a 1-bit DAC  $b = 1$ ,  $M = 32$ ,  $K = 1$  for MRT precoding for different user angles. Users are indicated by a star.

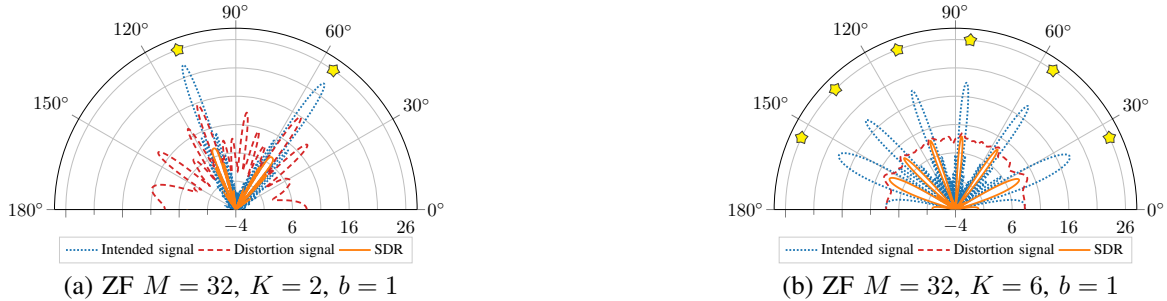


Fig. 4: Radiation pattern for ZF of the intended signal  $P_{\text{lin}}(\tilde{\phi})$ , distortion  $P_{\text{dist}}(\tilde{\phi})$  and SDR  $P_{\text{SDR}}(\tilde{\phi})$  in [dB] for a 1-bit DAC. Users are indicated by a star, the user angles are  $55^\circ, 110^\circ$  in (a) and  $\{25^\circ, 55^\circ, 85^\circ, 110^\circ, 135^\circ, 155^\circ\}$  in (b).

Each of the obtained probability vectors is a result of a softmax activation. The elements of these vectors can be interpreted as the parameters of a categorical distribution conditioned on  $\mathbf{H}$  and  $\mathbf{s}$ , where each category (output level in our case) is assigned a certain probability of being the correct output level. The logits/the raw outputs of the NN (i.e., the output before applying the softmax activation) for the real and imaginary parts of antenna  $m$  are defined as  $\mathbf{a}_{\mathcal{R},m}$ ,  $\mathbf{a}_{\mathcal{I},m}$  respectively. The softmax of vector  $\mathbf{a}_{\mathcal{R},m}$  is computed as<sup>2</sup>

$$[\mathbf{p}_{\mathcal{R},m}]_i = [\text{softmax}(\mathbf{a}_{\mathcal{R},m})]_i = \frac{e^{[\mathbf{a}_{\mathcal{R},m}]_i}}{\sum_j e^{[\mathbf{a}_{\mathcal{R},m}]_j}} \quad (19)$$

where  $[\text{softmax}(\mathbf{a}_{\mathcal{R},m})]_i$  is the  $i$ -th element of the softmax-transformed vector  $\mathbf{p}_{\mathcal{R},m}$ . This scales all values of  $\mathbf{a}_{\mathcal{R},m}$  between zero and one and ensures that the summation of all elements of the vector equals one, hence the output values of the softmax function can be interpreted as probabilities.

2) *Overcoming Non-Differentiability*: If we know the correct labels for  $\mathbf{p}_{\mathcal{R},m}, \mathbf{p}_{\mathcal{I},m}$  we can learn in a supervised manner by minimizing the cross entropy loss between the output of the softmax layers and the labels. Given that these labels are expensive to obtain, unsupervised training is used. We interpret the output of the softmax layer as the probability each output level has to be the 'best' value. To select the best output labels we take the argmax of these probability vectors to select the maximum likelihood output levels, as depicted in (18). The problem here is that the argmax function is non-differentiable. A common workaround is to use the argmax function in the forward pass of the NN and estimate

the gradients using a softmax function in the backward pass. However, empirically, we found this approach to give poor results, as it often leads to greedy, sub-optimal solutions [37]. Motivated by the exploration-exploitation dilemma, we aim to introduce more exploration by treating the output of the NN as the parameters of a categorical distribution, from which samples are drawn rather than selecting the maximum value via argmax. This sampling introduces a degree of exploration, enabling the NN to observe a wider variety of (potentially negative) examples during training. This enables the model to escape sub-optimal local minima. By contrast, relying on the deterministic argmax function emphasizes exploitation, which risks converging to greedy, suboptimal solutions [37].

To train the NN in this way a sampling scheme of which the gradients can be estimated is required. We use a relaxed reparameterization gradient estimator known as the straight-through Gumbel-softmax estimator [37], [44]. To build up to this we discuss three variants: (1) the Gumbel-max estimator, (2) the Gumbel-softmax estimator and (3) the straight-through Gumbel-softmax estimator. First, we consider a reparameterization gradient estimator (1). This estimator reparameterizes the sampling of a random variable by using a sample from a standard distribution combined with a deterministic transformation. In our case, this is referred to as the Gumbel-max trick, where a sample from the categorical distribution  $I \sim \text{cat}(\mathbf{p}_{\mathcal{R},m})$  is obtained by sampling the standard Gumbel distribution and then transforming it. More concretely, sampling the categorical distribution is equivalent to adding samples from the standard Gumbel distribution to the logits and selecting the index with the highest value [37]

$$I = \arg \max_{i \in \{0, \dots, L-1\}} \{[\mathbf{a}_{\mathcal{R},m}]_i + g_i\} \sim \text{cat}(\mathbf{p}_{\mathcal{R},m}) \quad (20)$$

<sup>2</sup>For the remainder of this discussion we will only refer to the real part of antenna  $m$ ,  $\mathbf{a}_{\mathcal{R},m}$ , however the same applies to the imaginary part  $\mathbf{a}_{\mathcal{I},m}$ .

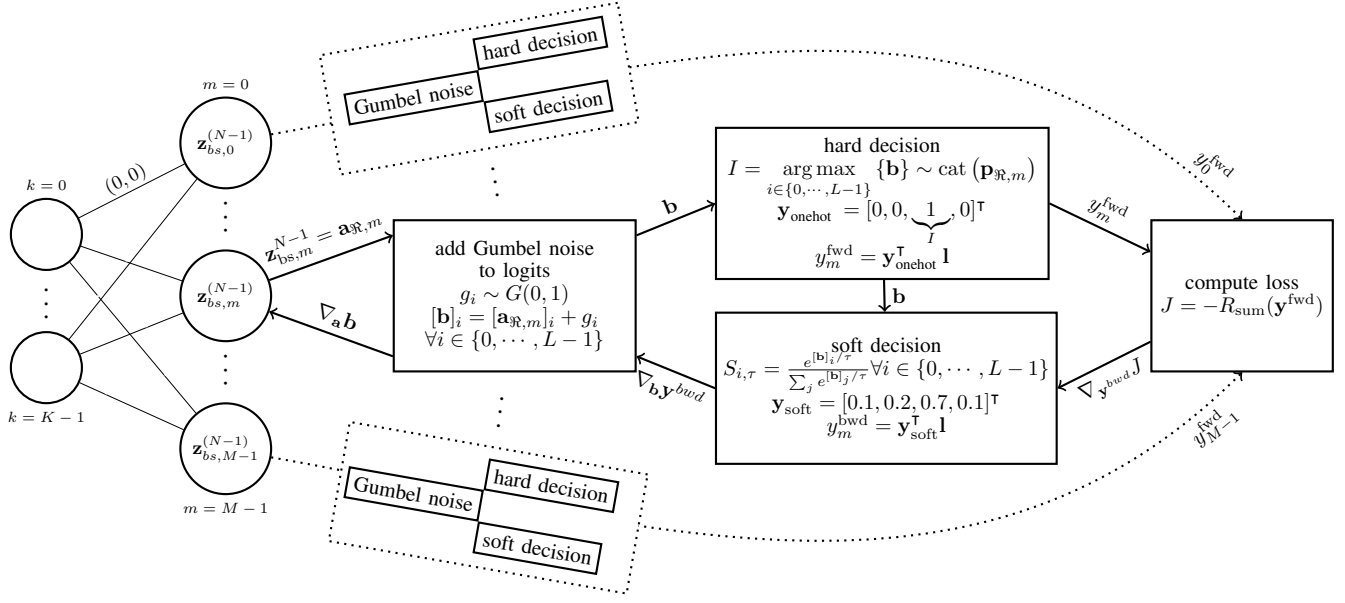


Fig. 5: Overview of the forward and backward pass during training. For clarity, only the real part is considered in this figure but the same applies for the imaginary part  $\mathbf{a}_{\Im,m}$ . The normalization step is omitted for simplicity. The vector  $\mathbf{1}$  contains all quantization levels, hence  $\mathbf{y}_{\text{onehot}}^{\text{T}} \mathbf{1}$  selects the desired output level. In this example,  $b = 2$  bits are considered, hence  $L = 4$ .

where  $g_i \sim \text{Gumbel}(0, 1)$  are samples from the standard Gumbel distribution and  $[\mathbf{a}_{\Re,m}]_i$  are unnormalized probabilities (i.e., the input to the softmax function as in (19)). However, for the Gumbel-max trick, the deterministic transformation is non-differentiable due to the argmax function. Therefore, a relaxed gradient estimator (2) is often used which replaces the argmax by a softmax function (typically with an added temperature variable  $\tau$ ). These soft samples are defined as

$$S_{i,\tau} = \frac{e^{([\mathbf{a}_{\Re,m}]_i + g_i)/\tau}}{\sum_j e^{([\mathbf{a}_{\Re,m}]_j + g_j)/\tau}} \quad \text{for } i \in \{0, \dots, L-1\}. \quad (21)$$

This approximates the (typically discrete) sample of the categorical distribution by a continuous random variable, which allows for the computation of gradients. This is known as the Gumbel-softmax trick. In the limit where  $\tau \rightarrow 0$  this converges to a discrete (one-hot encoded) sample  $\mathbb{1}_i^{|\mathcal{L}|}$ . For some applications, this relaxation is acceptable, however, given that the aim of this work is quantization, a continuous relaxation would undo the desired quantization. To overcome this, we use the straight-through Gumbel-softmax estimator (3). This estimator produces discrete samples in the forward pass and uses the gradients from the Gumbel-softmax trick in the backward pass. This can effectively be seen as using the Gumbel-max trick in the forward pass, and the Gumbel-softmax trick in the backward pass. An overview of this training procedure can be seen in Fig. 5. Note that, the straight-through Gumbel-softmax estimator is only used during training. At inference time, the argmax function is used to select the output levels that are assigned the highest probability according to (18), to obtain the precoded quantized vector  $\mathbf{y}$ .

### C. Neural Network Architecture

In this section, we discuss which type of NN architecture is adequate for non-linear precoding. Fully connected neural

networks, with 1 hidden layer and sufficient neurons, can approximate any continuous non-linear function with arbitrary accuracy [45]. This makes them theoretically capable of learning the desired function mapping concerning the problem considered in our work, i.e., a continuous mapping from channel matrix and symbol vector to probability vectors over the possible output levels of the DACs. Unfortunately, the universal approximation theorem is not constructive, i.e., it does not indicate how to choose the network architecture or the number of neurons required to achieve such accuracy. Given the universal function approximation theorem, the hypothesis space of a sufficiently large fully connected NN, that is the set of all possible functions the fully connected NN can represent, is theoretically infinite. While this expressive power is appealing, it introduces practical challenges. A larger hypothesis space increases the number of trainable parameters, making the network more difficult to train, data-hungry, and computationally expensive during inference. As such, in practice, it is advantageous to reduce the size of this hypothesis space in an informed manner. For a formal discussion of this mechanism, based on statistical learning theory, we refer to [24], [28], [29]. However, the main insight is as follows: by using certain NN architectures we restrict the NN to only learn certain groups of functions. As such, the hypothesis space of the NN is greatly reduced. This leads to more scalable NNs with fewer trainable parameters, which are easier to train and have lower computational complexity. This comes at the cost of a less expressive model, as the model can only learn the limited group of functions. The main idea lies in selecting the right NN architecture, which can learn a group of functions, which is known to cover the desired function. In this way, the reduction in expressivity does not affect the performance, as only functions outside of this group are ruled out. Next, we explain how this mechanism can be applied to our problem by

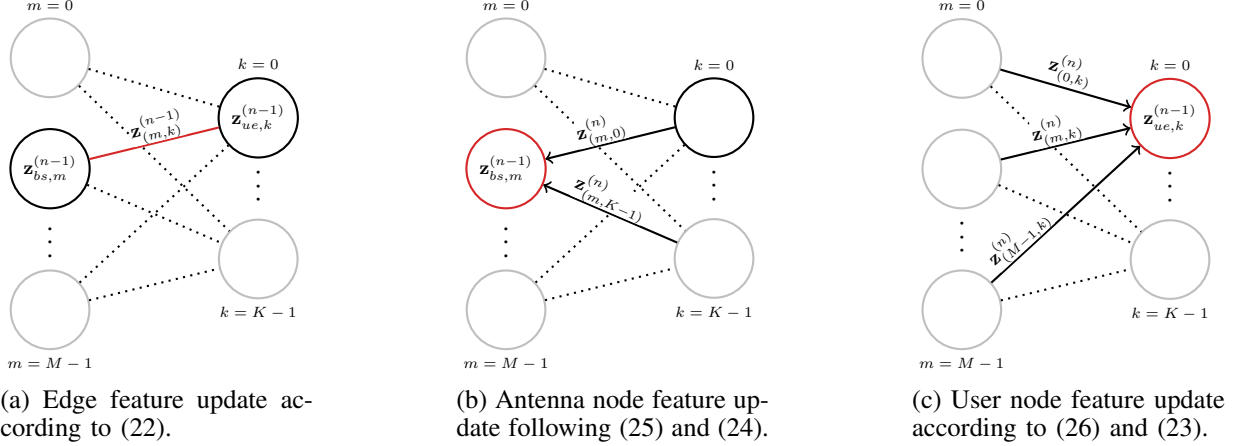


Fig. 6: GNN overview: antenna nodes are on the left, user nodes on the right. Red indicates the element being updated, black the elements used to perform that update. The previous value of the element, before the update, is also used during the update.

limiting the NN to only learn permutation equivariant/invariant functions.

For non-linear precoding, given the physical underlying system, the following equivariance and invariance properties need to be maintained. *i)* If the user order is permuted with permutation matrix  $\mathbf{\Pi} \in \{0, 1\}^{K \times K}$ , the output of the precoding function should remain unchanged, hence  $f(\mathbf{H}\mathbf{\Pi}, \mathbf{\Pi}\mathbf{s}) = \mathbf{y}_{\text{NL}}$ . The learned function should thus be permutation invariant with respect to the symbol vector and columns of the channel matrix. *ii)* If the antenna ordering is permuted with permutation matrix  $\mathbf{\Pi} \in \{0, 1\}^{M \times M}$ , the output of the precoding function should be permuted accordingly  $f(\mathbf{\Pi}\mathbf{H}, \mathbf{s}) = \mathbf{\Pi}\mathbf{y}_{\text{NL}}$ . The learned function should thus be permutation equivariant with respect to the rows of the channel matrix. When a NN imposes these properties on the learned functions, its hypothesis space is reduced as it can no longer learn all existing functions, but only the subset that respects these properties. Furthermore, this can only positively affect the learning performance, as the optimal function (i.e., a function that is permutation equivariant with respect to the antenna ordering, and permutation invariant with respect to the user ordering), is still covered by this restricted hypothesis space.

Next, a GNN architecture is described which respects these properties. The proposed GNN is based on generalized message passing [26], [46]. The GNN learns the mapping from channel matrix and symbol vector to a precoded and quantized vector over a graph. The graph in question has a node for each transmit antenna at the BS, a node for each user and an edge between each antenna and user as can be seen in Fig. 6a. The graph is defined as  $\mathcal{G} = (\mathcal{V}, \mathcal{E})$ , where  $\mathcal{V} = \mathcal{V}_M \cup \mathcal{V}_K$  is the set of nodes, with  $\mathcal{V}_M$  the antenna nodes and  $\mathcal{V}_K$  the user nodes, and  $\mathcal{E}$  the set of edges, which contains all edges between the antenna and user nodes i.e.,  $(m, k) \in \mathcal{E} \forall m \in \mathcal{V}_M, k \in \mathcal{V}_K$ . The graph is undirected, meaning that  $(m, k) \in \mathcal{E} \leftrightarrow (k, m) \in \mathcal{E}$ , as is the physical channel between each user and antenna. A general GNN performs a number of message-passing iterations. At iteration/layer  $n$ , a hidden representation is updated for each edge, antenna node, and user node, denoted by  $\mathbf{z}_{(m,k)}^{(n)}$ ,  $\mathbf{z}_{bs,m}^{(n)}$  and  $\mathbf{z}_{ue,k}^{(n)} \in \mathbb{R}^{d_n}$  respectively.

These representations are updated in layer  $n$  according to

$$\mathbf{z}_{(m,k)}^{(n)} = \sigma \left( \mathbf{W}_{\text{edge}}^{(n)} \mathbf{z}_{(m,k)}^{(n-1)} + \mathbf{W}_{\text{bs}}^{(n)} \mathbf{z}_{bs,m}^{(n-1)} + \mathbf{W}_{\text{ue}}^{(n)} \mathbf{z}_{ue,k}^{(n-1)} \right) \quad (22)$$

$$\mathbf{m}_{\mathcal{N}(k)} = \frac{1}{|\mathcal{N}(k)|} \sum_{m' \in \mathcal{N}(k)} \mathbf{z}_{(m',k)}^{(n)} \quad (23)$$

$$\mathbf{m}_{\mathcal{N}(m)} = \frac{1}{|\mathcal{N}(m)|} \sum_{k' \in \mathcal{N}(m)} \mathbf{z}_{(m,k')}^{(n)} \quad (24)$$

$$\mathbf{z}_{bs,m}^{(n)} = \sigma \left( \mathbf{W}_{\text{self,bs}}^{(n)} \mathbf{z}_{bs,m}^{(n-1)} + \mathbf{W}_{\text{neigh,bs}}^{(n)} \mathbf{m}_{\mathcal{N}(m)} \right) \quad (25)$$

$$\mathbf{z}_{ue,k}^{(n)} = \sigma \left( \mathbf{W}_{\text{self,ue}}^{(n)} \mathbf{z}_{ue,k}^{(n-1)} + \mathbf{W}_{\text{neigh,ue}}^{(n)} \mathbf{m}_{\mathcal{N}(k)} \right). \quad (26)$$

Here  $\sigma(\cdot)$  is a non-linear activation and the matrices  $\mathbf{W}_{\text{edge}}^{(n)}, \mathbf{W}_{\text{bs}}^{(n)}, \mathbf{W}_{\text{ue}}^{(n)}, \mathbf{W}_{\text{self,bs}}^{(n)}, \mathbf{W}_{\text{self,ue}}^{(n)} \in \mathbb{R}^{d_n \times d_{n-1}}$  and  $\mathbf{W}_{\text{neigh,bs}}^{(n)}, \mathbf{W}_{\text{neigh,ue}}^{(n)} \in \mathbb{R}^{d_n \times d_n}$  are learned. The dimensions of these matrices ( $d_{n-1}, d_n$ ) determine the number of features in layer  $n-1$  and  $n$  respectively. Note that  $m$  denotes the antenna index,  $k$  the user index and  $(m, k)$  the edge between antenna  $m$  and user  $k$ . First, in (22) the edge features are updated according to the edge, antenna and user features from the previous layer. Second, in (23) message passing is performed from the neighbors of each user node to generate the user messages, in (24) message passing is performed from the neighbors of each antenna node to generate the antenna messages. Next, in (25) the antenna features are updated according to the antenna messages and the antenna features from the previous layer. Finally, in (26) the user features are updated according to the user features from the previous layer and the user messages. Figure 6 provides an overview of these computations. Note that these operations are repeated for a total of  $N$  layers: one input layer, one output layer and  $N_h = N - 2$  hidden layers.

The inputs for edge  $(m, k)$ , antenna node  $m$  and user node  $k$  in layer one of the GNN are defined in the following way

$$\mathbf{z}_{(m,k)}^{(0)} = [\Re\{\mathbf{H}\}_{m,k}, \Im\{\mathbf{H}\}_{m,k}]^T \quad (27)$$

$$\mathbf{z}_{bs,m}^{(0)} = [0, 0]^T \quad (28)$$

$$\mathbf{z}_{ue,k}^{(0)} = [\Re\{s_k\}, \Im\{s_k\}]^T. \quad (29)$$



The outputs of the GNN are the precoded symbols, which are defined as the antenna node features in the final layer

$$\mathbf{z}_{bs,m}^{(N-1)} = [\Re\{y_m\}, \Im\{y_m\}]^T. \quad (30)$$

Note, however, that the actual outputs of the GNN are probability vectors as discussed in the previous section  $\mathbf{z}_{bs,m}^{(N-1)} = [\mathbf{p}_{\Re,m}, \mathbf{p}_{\Im,m}]^T$ . At inference time, these probability vectors are mapped to the precoded symbols according to (18).

## V. COMPLEXITY ANALYSIS

In this section, the complexity of the proposed GNN is computed in terms of real floating point operations (FLOPs).

### A. Complexity of the GNN

The forward pass of the GNN is described in equations (22), (23), (24), (25) and (26). To compute the complexity, a distinction is made between the input layer, the four hidden layers ( $N_h = 4$ ) and the output layer, as the dimensions of the inputs, the features, and the outputs are different in each of these layers. In the input layer  $d_0 = 2$ , in the hidden layers  $d_n = d_h = 128 \forall n \in \{1, \dots, N-2\}$  and in the output layer  $d_{N-1} = 2^{b+1}$ . Additionally, (22) has to be computed for each edge ( $MK$  times), (23) and (26) for each user node ( $K$  times) and (24) and (25) for each antenna node ( $M$  times).

For the input layer, the number of real floating-point multiplications is

$$\begin{aligned} \mathcal{O}_{\text{in}}^{(\text{mul})} &= \underbrace{6MKd_h}_{(22)} + \underbrace{Kd_h}_{(23)} + \underbrace{Md_h}_{(24)} \\ &+ \underbrace{2Md_h + Md_h^2}_{(25)} + \underbrace{2Kd_h + Kd_h^2}_{(26)} \end{aligned} \quad (31)$$

and the number of real floating-point additions is

$$\begin{aligned} \mathcal{O}_{\text{in}}^{(\text{add})} &= \underbrace{5MKd_h}_{(22)} + \underbrace{K(M-1)d_h}_{(23)} + \underbrace{M(K-1)d_h}_{(24)} \\ &+ \underbrace{Md_h + Md_h^2}_{(25)} + \underbrace{Kd_h + Kd_h^2}_{(26)}, \end{aligned} \quad (32)$$

where the underbraces indicate the equations that require the indicated computations. One hidden layer requires

$$\mathcal{O}_h^{(\text{mul})} = \underbrace{3MKd_h^2}_{(22)} + \underbrace{Kd_h}_{(23)} + \underbrace{Md_h}_{(24)} + \underbrace{2Md_h^2}_{(25)} + \underbrace{2Kd_h^2}_{(26)} \quad (33)$$

real floating-point multiplications and

$$\begin{aligned} \mathcal{O}_h^{(\text{add})} &= \underbrace{3MKd_h^2 - MKd_h}_{(22)} + \underbrace{K(M-1)d_h}_{(23)} + \underbrace{M(K-1)d_h}_{(24)} \\ &+ \underbrace{2Md_h^2 - Md_h}_{(25)} + \underbrace{2Kd_h^2 - Kd_h}_{(26)} \end{aligned} \quad (34)$$

real floating-point additions. For the output layer, only the antenna node features are computed as they are the final output of the GNN. This requires

$$\mathcal{O}_{\text{out}}^{(\text{mul})} = \underbrace{6MKd_h2^b}_{(22)} + \underbrace{2M2^b}_{(24)} + \underbrace{4M2^{2b} + 2Md_h2^b}_{(25)} \quad (35)$$

real floating-point multiplications and

$$\begin{aligned} \mathcal{O}_{\text{out}}^{(\text{add})} &= \underbrace{6MKd_h2^b - 2MK2^b}_{(22)} \\ &+ \underbrace{2M(K-1)2^b}_{(24)} + \underbrace{4M2^{2b} + 2Md_h2^b - 2M2^b}_{(25)} \end{aligned} \quad (36)$$

real floating-point additions. In total, the GNN with  $N_h = 4$  requires the following number of floating-point multiplications

$$\mathcal{O}_{\text{GNN}}^{(\text{mul})} = \mathcal{O}_{\text{in}}^{(\text{mul})} + N_h \mathcal{O}_h^{(\text{mul})} + \mathcal{O}_{\text{out}}^{(\text{mul})} \quad (37)$$

and the following number of floating-point additions

$$\mathcal{O}_{\text{GNN}}^{(\text{add})} = \mathcal{O}_{\text{in}}^{(\text{add})} + N_h \mathcal{O}_h^{(\text{add})} + \mathcal{O}_{\text{out}}^{(\text{add})} \quad (38)$$

This scales as  $\mathcal{O}(d_h^2 MK + 2^b MKd_h + 2^{2b} M)$  multiplications and  $\mathcal{O}(d_h^2 MK + 2^b MKd_h + 2^{2b} M)$  additions.

## VI. SIMULATION RESULTS

### A. Training Parameters and Simulation Setup

For the following simulations, the total transmit power is normalized to  $P_T = M$ . During training, the signal-to-noise ratio (SNR) is fixed at  $P_T/\sigma_v^2 = 20$  dB. All models are trained for 20 epochs unless specified otherwise. The batch size is set to 128, the Adam optimizer [43] is used with a learning rate of  $5 \times 10^{-3}$ . During training, the loss function in (13) is computed numerically. Hence, per channel,  $N_s = 125$  complex Gaussian symbols are generated per user according to  $s_k \sim \mathcal{CN}(0, 1)$ . These symbols are precoded and quantized for the current channel using the GNN. For this, non-uniform quantization levels are used, which are obtained using the Max-Lloyd algorithm, as described in Section II-B2. Next, the average power constraint is enforced by performing a scalar normalization over these  $N_s = 125$  symbols according to (15). Finally, these precoded and quantized symbols ( $\mathbf{y}_{\text{NL}}$ ), are used together with the intended transmit symbols ( $\mathbf{s}$ ), to evaluate the expectation in the loss function according to (13). The training set consists of 200 000 generated channels, each of which is accompanied by  $N_s = 125$  symbol vectors. The channels are sampled from a complex normal distribution  $[\mathbf{H}]_{i,j} \sim \mathcal{CN}(0, 1)$  if a Rayleigh fading channel is assumed. However, when constructing radiation patterns, a LOS channel is considered according to (10), where the user angle (in degrees) is randomly sampled from a discrete uniform distribution  $\phi_k \sim \mathcal{U}\{0, 180\}$ . All NN hyperparameters are selected on a validation set of 1000 channel realizations, while the simulation results are obtained on an independent test set of 10 000 channel realizations. The GNN used in this section contains one input layer, four hidden layers ( $N_h = 4$ ), one output layer and  $d_h = 128$  features are learned in the hidden layers unless specified otherwise. The non-linear activation function in all hidden layers is the leaky rectified linear unit (LReLU) which is defined as  $\sigma(a) = \max(0, a) - 0.01\min(0, a)$ . Finally, the temperature of the Gumbel-softmax estimator is set to  $\tau = 1$ .

### B. GNN-Based Non-Linear Precoding Single-User Case

In this section, the performance of the proposed GNN-based non-linear precoder is evaluated for the single-user case. In Fig. 7a the rate is depicted for a varying SNR ( $= P_T/\sigma_v^2$ ) for  $M = 32$  transmit antennas,  $K = 1$  user and a varying number of bits  $b \in \{1, 2, 3, 4\}$ . From this figure, it is clear

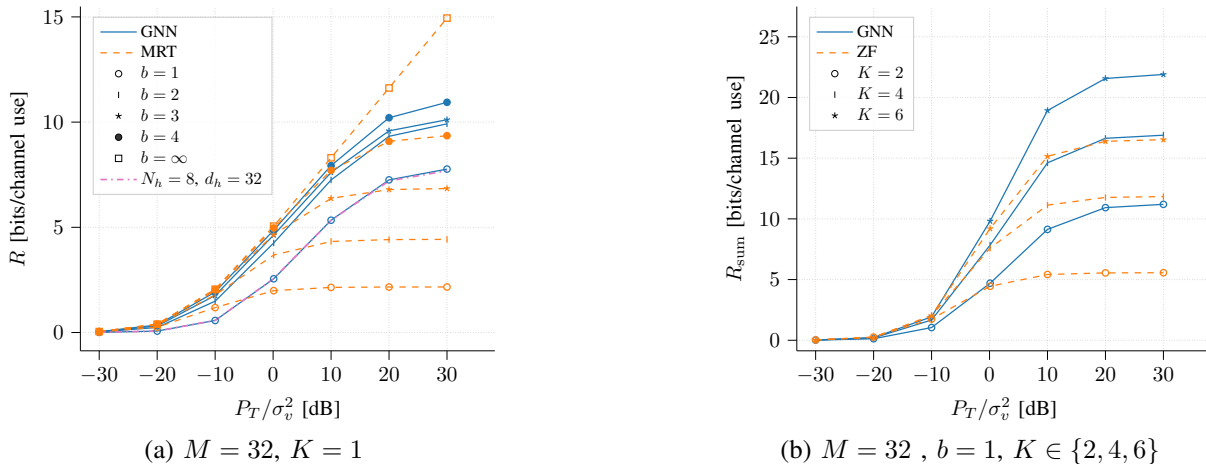


Fig. 7: Achievable rates averaged over the channel realizations taken from the test set. Comparing the GNN non-linear precoder against MRT or ZF, for the single-user case and a varying number of bits (a) and the multi-user case with one bit and a varying number of users (b).

that the GNN outperforms MRT precoding in the distortion-limited regime i.e., at high SNR. At high SNR, the GNN with one bit DACs delivers slightly better performance than MRT with three bit DACs. This highlights the ability of the GNN-based precoder to leverage over-the-air combining to provide a higher-quality signal. Next to this, the GNN outperforms classical linear precoding for one to four bit DACs. However, the performance gap decreases as the number of bits goes up. This is to be expected for two reasons: *i*) as the number of bits rises, the distortion goes down, hence there is less to gain by using quantization-aware precoding and *ii*) the problem complexity increases, as the number of possible output levels rises exponentially with the number of bits, this increased search space results in a harder problem to solve. In conclusion, in the single-user case, the proposed method outperforms classical MRT precoding for one to four bits. However, the gains are most pronounced in the one-bit case.

In Fig. 8, the radiation pattern of MRT is compared to the GNN for the one-bit single-user case  $b = 1$ ,  $K = 1$ . This figure highlights that the GNN achieves its gain by sending the distortion in non-user directions, while the distortion in the user direction is kept to a minimum. This results in a higher SDR in the user direction as compared to MRT, as can be seen in Fig. 8c. In Fig. 9 the radiation pattern is depicted for the one-bit single-user case  $b = 1$ ,  $K = 1$  where the number of transmit antennas is varied  $M \in \{8, 16, 32\}$ . Given the increase in degrees of freedom when the number of transmit antennas grows, the GNN can control both the intended signal and distortion more precisely. This leads to an increase in SDR in the user direction as the number of transmit antennas increases.

In Fig. 10a the transmitted symbols  $s$  are plotted in function of the estimated received symbols  $\hat{s}$  for  $M = 2$  transmit antennas,  $K = 1$  user and  $b = 1$  bit. In general, for complex channels and transmit symbols, after over-the-air combining,  $2^{2bM}$  possible symbols can be received. These possible received signals are not uniformly distributed but depend on the channel realizations and the transmit signal at each antenna. Hence, selecting the right transmit signal at each antenna allows for control over the received signals. However,

TABLE I: NMSE for MRT and GNN on all (noiseless) channels and symbols from the test set, for  $M = 32$ ,  $K = 1$ .

Precoder	$b = 1$	$b = 2$	$b = 3$	$b = 4$
NMSE MRT [dB]	-5.38	-13.02	-20.31	-27.70
NMSE GNN [dB]	-22.99	-29.43	-29.87	-32.52

this is limited by the values of each channel realization. Nevertheless, Fig. 10a, illustrates that the GNN can more effectively utilize these 16 possible symbols after over-the-air combining to obtain a good estimate close to the transmitted symbol. This is illustrated by the difference in normalized mean squared error (NMSE), which is computed as  $\text{NMSE} = \frac{\mathbb{E}(|s - \hat{s}|^2)}{\mathbb{E}(|s|^2)}$ . The GNN achieves a NMSE of -10.11 dB, and MRT a NMSE of -7.43 dB. This increased performance scales with the number of transmit antennas as after over-the-air combining,  $2^{2bM}$  possible symbols can be received. In Fig. 10b the transmitted symbols  $s$  are plotted in function of the estimated received symbols  $\hat{s}$  for  $M = 32$  transmit antennas,  $K = 1$  user and  $b = 1$  bit DACs. For MRT, the estimated symbols differ largely from the transmitted symbols. When using GNN-based non-linear precoding a remarkable improvement can be observed. This is expected given the increase in transmit antennas, which leads to  $2^{2bM} = 2^{64}$  possible received symbols. This demonstrates the potential of using many transmit antennas in combination with one bit DACs. However, the challenge lies in selecting the right combination of DAC output levels at each transmit antenna to obtain the desired received signal. Figure 10b demonstrates the ability of the GNN to select the correct output levels at each DAC which results in estimated symbols that match very closely the transmit symbols. To quantify this, the NMSE is computed over all noiseless channel realizations and symbols from the test set. This is done for MRT and GNN precoding for  $b \in \{1, 2, 3, 4\}$  bits in Table I. For one-bit DACs the GNN achieves a NMSE of -22.99 dB, while MRT leads to a NMSE of -5.38 dB, highlighting the performance gap between MRT and the GNN. As the number of bits increases, this performance gap decreases. However, even for  $b = 4$  bits, the GNN achieves a NMSE of -32.52 dB, while MRT precoding achieves a NMSE of -27.70 dB.

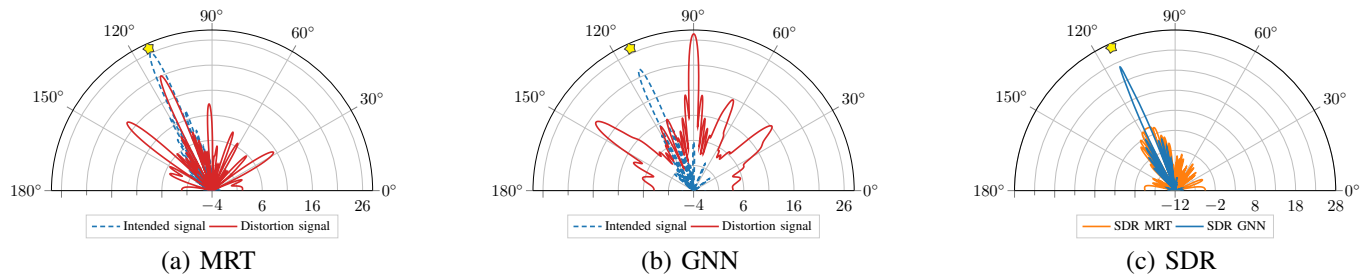


Fig. 8: Radiation pattern of the intended signal  $P_{\text{lin}}(\tilde{\phi})$  and distortion signal  $P_{\text{dist}}(\tilde{\phi})$  [dB] for a 1-bit DAC,  $M = 32$  and  $K = 1$ . The GNN precoder (a) and MRT precoding (b) are compared for a pure LOS channel and a half-wavelength ULA. The user is indicated by a star. In (c) the signal-to-distortion ratio (SDR) radiation pattern  $P_{\text{SDR}}(\phi)$  is depicted [dB].

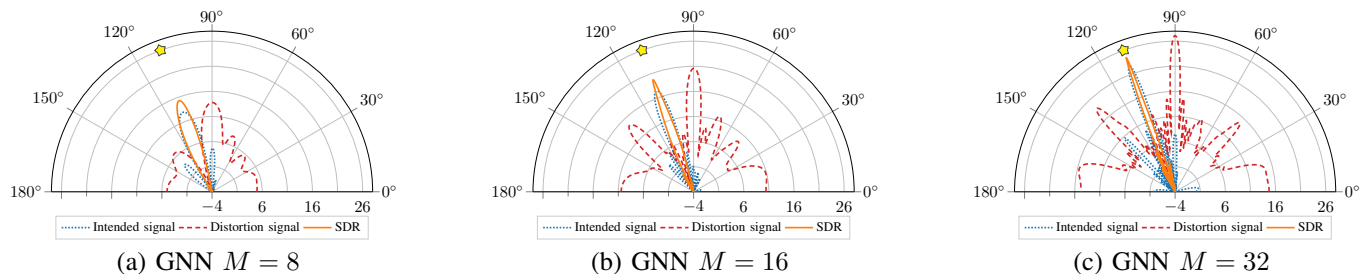


Fig. 9: Radiation pattern of the GNN for the intended signal  $P_{\text{lin}}(\tilde{\phi})$  and distortion signal  $P_{\text{dist}}(\tilde{\phi})$  [dB] for a 1-bit DAC, varying number of transmit antennas  $M \in \{8, 16, 32\}$  and  $K = 1$  user. The user angle is  $\phi = 110^\circ$ .

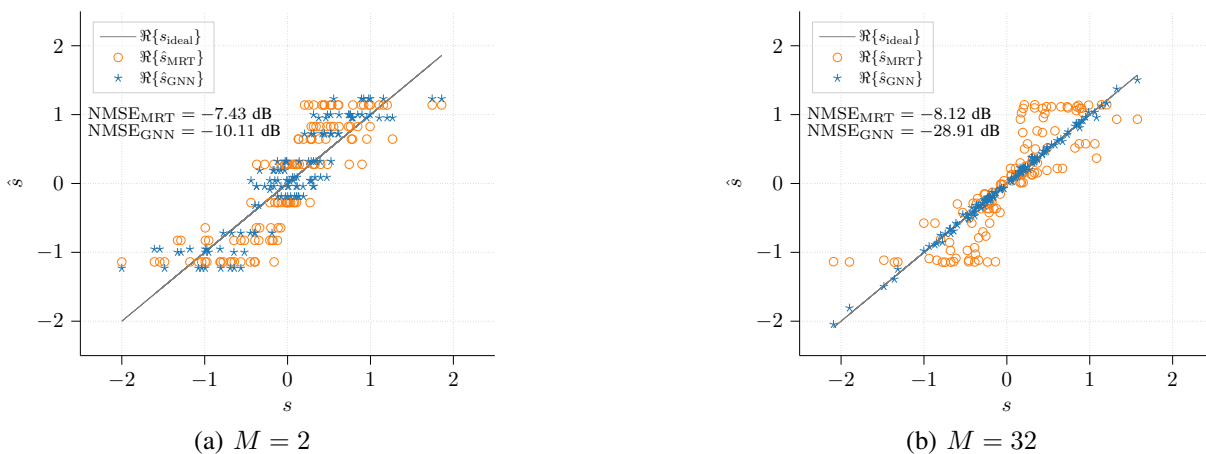


Fig. 10: Real part of the estimated symbol  $\hat{s}$  in function of the transmitted symbol  $s$ , over a single realization of a noiseless Rayleigh fading channel. Comparing MRT with GNN precoding, for  $M = 2$  (a) and  $M = 32$  (b),  $K = 1$  and  $b = 1$ .

### C. GNN-Based Non-Linear Precoding Multi-User Case

In this section, the proposed precoder is evaluated in the multi-user scenario. In Fig. 7b the sum rate in function of the SNR is depicted for  $M = 32$  transmit antennas,  $b = 1$  bit and a varying number of users  $K \in \{2, 4, 6\}$ . This figure shows that the GNN outperforms ZF in the distortion-limited regime, i.e., at high SNR. As the number of users increases, the distortion receives less of a beamforming gain, and as such becomes more spatially spread out. Consequently, there is less to gain in terms of system performance. Additionally, this reduced gain is explained by the fact that the more users are present, the harder it is to train the GNN.

In Fig. 11, the sum rate is illustrated in function of the

number of bits for a fixed SNR =  $P_T/\sigma_v^2 = 20$  dB, for  $M = 32$  transmit antennas and  $K \in \{1, 2, 4, 6\}$  users. When comparing the GNN precoder with the baseline (MRT or ZF) it is clear that the proposed method is most performant when few users are present and few bits are considered. When more users are present and/or more bits are considered, the proposed method shows similar or lower performance than the baseline. This is expected as the potential gains diminish as the number of users increases, and as the complexity of the problem exponentially increases with the number of bits. Note that in Fig. 11 two GNNs are considered, the standard model with  $d_h = 128$  features and a bigger model with  $d_h = 256$  features. When the problem complexity is higher, i.e., more bits and users

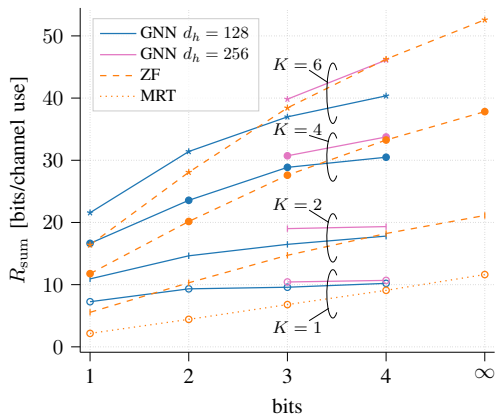


Fig. 11: Achievable rates on test set,  $P_T/\sigma_v^2 = 20$  dB. Comparing GNN and MRT or ZF for  $M = 32$ ,  $K \in \{1, 2, 4, 6\}$ . A bigger GNN ( $d_h = 256$ ) is added for  $b \in \{3, 4\}$ .

are considered, it is shown that the larger GNN ( $d_h = 256$ ) achieves better performance as compared to the smaller model ( $d_h = 128$ ) and ZF precoding. However, this comes at the cost of an increased model size and complexity. Nevertheless, previously the most critical case was identified as the one with few users and few bits, in this regime, the proposed smaller model ( $d_h = 128$ ) outperforms the baseline.

## VII. POWER CONSUMPTION

To quantify the power consumption of the proposed precoder, the consumed power of the DACs and the processing due to the GNN is taken into account.

### A. DACs Power Consumption

We consider the widely used current steering DAC architecture, with the following power consumption model [4]

$$P_{\text{DAC}} \approx \frac{1}{2} V_{dd} I_0 (2^b - 1) + b C_p \frac{f_s}{2} V_{dd}^2 \quad (39)$$

where  $V_{dd}$  is the supply voltage,  $I_0$  the current of the current source of the least significant bit and  $C_p$  the parasitic capacitance of each transistor. Based on [4] we use  $V_{dd} = 3$  V,  $I_0 = 10$   $\mu$ A and  $C_p = 1$  pF.

For a fair comparison of the consumed power, a fixed quality of service is selected at which the proposed precoder is compared to the conventional precoder. As a concrete example, a rate constraint of 7 bits/channel use is considered for the scenario in Fig. 7a at an SNR = 20 dB. From this figure, it is clear that the GNN can meet this constraint by using DACs with  $b = 1$  bits while MRT requires  $b = 3$  bits. Given the required bit resolution and sampling frequency, the consumed power of all DACs is  $P_{\text{DACs,tot}} = 2M P_{\text{DAC}}$ . Note that we here consider two types of DACs, namely the classical baseband DAC, whereby the system relies on analog upconversion to place the signal at the desired carrier frequency and the RF-DAC which directly synthesizes the signal at the desired carrier frequency. For the classical baseband DAC we consider a sampling frequency of  $f_s = 4B$ , where  $B$  is the bandwidth and an oversampling factor of four is applied. For the RF-DAC we select  $f_s = 4f_c/(2n-1)$ , which places the baseband signal at the center of the  $n^{\text{th}}$  Nyquist zone. In practice, the second Nyquist zone ( $n = 2$ ) is most commonly utilized [5]. Note that for the RF-DAC the sampling frequency is independent

of the bandwidth, however, the condition  $f_s \geq B$  must be satisfied, which is generally the case, hence  $f_s = \frac{4}{3} f_c$ . The consumption of the baseband DACs is illustrated in Fig. 12 in function of the bandwidth  $B$ . The proposed precoder allows the DACs to consume a factor of 4-7 less power. In Fig. 13 the power consumption of the RF-DACs is given as a function of the bandwidth. Note that this consumption is constant over the bandwidth as the sampling frequency for the RF-DAC is linked to the carrier frequency  $f_c = 3.5$  GHz, rather than the bandwidth. The proposed precoder allows the RF-DACs to consume a factor of 3 less power as compared to MRT. This is to be expected as the power consumption of the RF-DACs is dominated by the dynamic consumption (term 2 in (39)), which scales linearly with the number of bits, while the sampling frequency is fixed for both precoders.

### B. GNN Processing Power Consumption

As computed in Section V, the total number of FLOPs required to run the GNN one time is  $\mathcal{O}_{\text{GNN}}^{(\text{add})} + \mathcal{O}_{\text{GNN}}^{(\text{mul})}$ . However, given that non-linear precoding is considered, the GNN needs to be executed for each transmit symbol. Hence, to compute how many forward passes are required per second, the symbol rate is computed. Consider a transmission bandwidth  $B = (1 + \alpha_{\text{rol}})/T$ , where  $T$  is the symbol period and  $\alpha_{\text{rol}} = 0.1$  a roll-off factor. This gives a symbol rate of  $R_s = \frac{B}{1 + \alpha_{\text{rol}}}$  symbols per second. Given this, the GNN needs to precode  $R_s$  symbols per second. Hence the total time complexity of the GNN is  $R_s (\mathcal{O}_{\text{GNN}}^{(\text{add})} + \mathcal{O}_{\text{GNN}}^{(\text{mul})})$  FLOPs per second. Given this, we can compute the required speed of the accelerator given a certain bandwidth. For instance, when considering  $B = 1$  MHz the considered accelerator requires a speed of 12 TFLOPs/second. Based on the NN accelerator comparison from [47], we select the accelerator from [48] that achieves the speed requirement of 12 TFLOPs/s and has a high efficiency of  $\eta = 646.6$  TFLOPs/s/W. This accelerator operates on 8-bit floating point numbers while the current GNN is trained on 32-bit floating point numbers. The influence of this reduced precision on the performance of the GNN should be further investigated. Nevertheless, to get an estimate of the achievable power consumption of the GNN processing, it is expressed in function of the bandwidth as  $P_{\text{GNN}} = \frac{1}{\eta} \frac{B}{1 + \alpha_{\text{rol}}} (\mathcal{O}_{\text{GNN}}^{(\text{add})} + \mathcal{O}_{\text{GNN}}^{(\text{mul})})$ . First we consider the baseband DACs, from Fig. 12 it can be noted that the proposed solution provides a power reduction when the system bandwidth is below 200 kHz. When the bandwidth is further increased, the gain of using fewer bits in the DACs is overshadowed by the increased GNN processing power consumption. However, by noting that the computational complexity of the GNN in (37) and (38) scales linearly with the number of layers  $N_h$  but quadratically with the number of features  $d_h$ , the processing power consumption can be reduced. By, changing the depth and width of the GNN to  $N_h = 8$ ,  $d_h = 32$  rather than  $N_h = 4$ ,  $d_h = 128$ , the performance (for  $K = 1$ ,  $b = 1$ ) is maintained while the power consumption is drastically reduced, as can be seen in Fig. 7a and Fig. 12. This results in a power reduction for a system bandwidth up to 3.5 MHz. Note that the speed requirement for the GNN with  $N_h = 8$ ,  $d_h = 32$  is still met, as the selected accelerator from [48] has a maximum speed of 39.8 TFLOPs/s, while at  $B = 4$  MHz the GNN, requires 8.82 TFLOPs/s. Next to this, we study the power consumption when considering RF-DACs in Fig. 13. The consumption of RF-DACs is much larger as compared to baseband DACs, hence the added consumption of the GNN

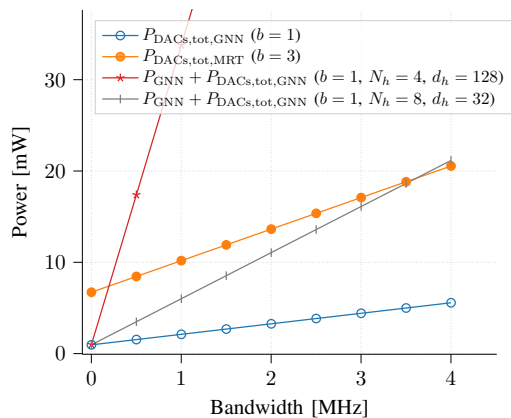


Fig. 12: Power consumption of the DACs and GNN processing in function of the bandwidth.

processing is minor as compared to the RF-DAC consumption. This leads to power savings, which are maintained for much higher bandwidths. However, in this situation, the limiting factor is the speed of the NN accelerator rather than its power consumption. The accelerator from [48] has a maximum speed of 39.8 TFLOPs/s. This limits the maximum bandwidth when using the GNN with  $N_h = 4$ ,  $d_h = 128$  to 1.95 MHz<sup>3</sup> while the maximum achievable bandwidth for the GNN with  $N_h = 8$ ,  $d_h = 32$  is 15.8 MHz. Nevertheless, over the 15.8 MHz bandwidth, a power reduction of 2.9 is maintained. As a perspective, future work could investigate more in-depth the performance and power consumption trade-off for the optimal GNN structure.

Additionally, it is worth noting that, the current analysis only considers the increase in GNN power consumption and the decrease in DACs power consumption, while other factors might be at play. For instance, the reduced resolution could have auxiliary effects as the power consumption in the digital chain can be reduced when this lower resolution is exploited, e.g., the power consumption of digital filters can be reduced as fewer bits need to be computed. Moreover, the power consumption of the digital fronthaul, which connects the baseband unit with the antenna array, can also be reduced when fewer bits are required. This could allow a large energy reduction, especially in a distributed/cell-free scenario where long fronthaul connections may connect central processing units to access points. These indirect effects should be considered in a further analysis.

## VIII. PRACTICAL IMPLEMENTATION CHALLENGES

While the proposed methods are promising in terms of system-level performance, practical deployment raises several challenges. Given that the proposed method relies on non-linear precoding, the computational complexity is linked to the symbol rate and hence, the system bandwidth. Consequently, the current system is limited to bandwidths of 15.8 MHz due to the limited processing speed of the current state-of-the-art hardware accelerator. However, given the rapid advancements in hardware accelerators driven by growing demand for NN applications, the speed and efficiency of these hardware accelerators are expected to improve further [47]. Furthermore, training and deployment raise several challenges. The base

<sup>3</sup>Note that for completeness the expected power consumption for higher bandwidths is also added to Fig. 13.

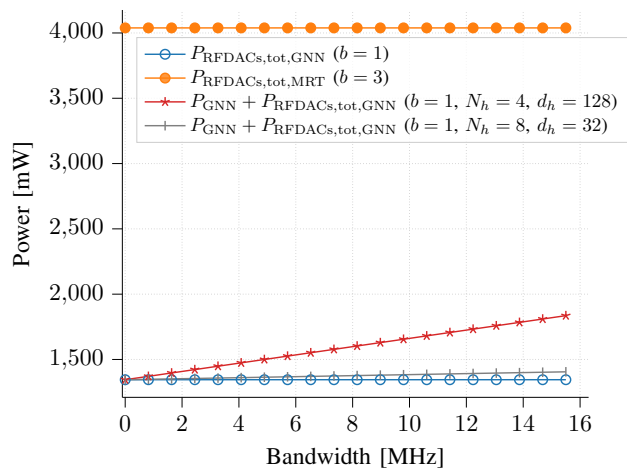


Fig. 13: Power consumption of the RF-DACs and GNN processing in function of the bandwidth.

model could be trained on simulation data (generated channels in our case). However, the distribution of the real-life measured channels will be different from the simulated channels. In the literature, this phenomenon is known as covariate shift [49]. Even so, by training in a simulated environment, a good initialization point of the model can be obtained, which can then be further fine-tuned using a limited set of measured real-life data [49]. By pre-training the model on simulation data, the amount of real-life measurements, which are often expensive and time-consuming to collect, can be limited [49]. Once deployed, another challenge arises, namely, maintaining the model when the data distribution varies over time. For instance, the properties of the wireless environment can change due to changes in the physical environment. Hence, the model needs to be continually updated. However, a trade-off arises here to avoid the problem known as catastrophic forgetting, where updating the model on new data usually results in a severe performance degradation on the old data [50]. To overcome these challenges, we refer to the rich literature on continual learning [50]. Finally, the proposed models should be compliant with current standards. As it stands, machine learning models are not standardized [51]. However, testability and consistent system behavior are concerns. Hence, these models should be extensively tested to meet current standards. More specifically, related to this work practical constraints such as the adjacent channel leakage ratio (ACLR) might be problematic due to the non-linear behavior of the DACs. Such constraints could be incorporated into the loss function, during training, to be compliant with the current standard.

## IX. CONCLUSION

In this work, a coarsely quantized downlink massive MIMO system is considered. A GNN is proposed which leverages the many antennas at the BS to transmit the non-linear quantization distortion in non-user directions. By doing so, a significant increase in achievable sum rate is obtained. For instance, when considering one-bit quantization in the single user case at high SNR, a three times increase in achievable rate as compared to classical precoding is obtained. This allows for using DACs with fewer bits to achieve a similar sum rate as traditional precoding techniques, which require more bits. The power consumption of baseband DACs is reduced by a factor of 4-7. However, when considering the additional

processing power consumption, the total power reduction is only valid for bandwidths up to 3.5 MHz. Additionally, the power consumption of RF-DACs is reduced by a factor of 3. However, due to their higher absolute power consumption, the impact of the additional processing power consumption is limited, as the total power consumption is still reduced by a factor of 2.9. Next to this, a more holistic power consumption analysis, including the full digital chain and fronthaul consumption, can further improve these results. Moreover, future work should address the high processing power. For this two options remain open. *i*) The proposed solution can be further optimized by studying smaller GNN architectures, combined with model pruning and quantization of the model weights and activations. By doing so, the computational complexity of the current model can be significantly reduced. *ii*) The proposed solution relies on non-linear precoding. As such, the computational complexity scales linearly with the system bandwidth, which is the critical issue concerning the high processing power. Although challenging, future work could investigate this issue by using linear precoding and/or reduced-complexity non-linear precoders, which significantly reduce the computational complexity. Finally, the impact of channel estimation errors on the performance of the proposed method should be investigated.

#### REFERENCES

- [1] E. Björnson, L. Sanguinetti, H. Wymeersch, J. Hoydis, and T. L. Marzetta, "Massive mimo is a reality—what is next?: Five promising research directions for antenna arrays," *Digital Signal Processing Special Issue on Source Localization in Massive MIMO*, vol. 94, pp. 3–20, 2019.
- [2] E. G. Larsson, O. Edfors, F. Tufvesson, and T. L. Marzetta, "Massive MIMO for next generation wireless systems," *IEEE Communications Magazine*, vol. 52, no. 2, pp. 186–195, 2014.
- [3] A. Shafiq, N. Yang, C. Han, J. M. Jornet, M. Juntti, and T. Kürner, "Terahertz Communications for 6G and Beyond Wireless Networks: Challenges, Key Advancements, and Opportunities," *IEEE Network*, vol. 37, no. 3, pp. 162–169, 2023.
- [4] S. Cui, A. Goldsmith, and A. Bahai, "Energy-constrained modulation optimization," *IEEE Transactions on Wireless Communications*, vol. 4, no. 5, pp. 2349–2360, 2005.
- [5] L. H. Crockett, D. Northcote, and R. W. Steward, Eds., *Software defined radio with Zynq Ultrascale+ RFSoc*, 1st ed. Strathclyde Academic Media, 2023. [Online]. Available: <https://www.RFSocBook.com>
- [6] A. van den Bosch, M. Steyaert, and W. Sansen, "SFDR-bandwidth limitations for high speed high resolution current steering CMOS D/A converters," in *ICECS'99. Proceedings of ICECS '99. 6th IEEE International Conference on Electronics, Circuits and Systems (Cat. No.99EX357)*, vol. 3, 1999, pp. 1193–1196 vol.3.
- [7] L. Fan, S. Jin, C.-K. Wen, and H. Zhang, "Uplink Achievable Rate for Massive MIMO Systems With Low-Resolution ADC," *IEEE Communications Letters*, vol. 19, no. 12, pp. 2186–2189, 2015.
- [8] O. Orhan, E. Erkip, and S. Rangan, "Low power analog-to-digital conversion in millimeter wave systems: Impact of resolution and bandwidth on performance," in *2015 Information Theory and Applications Workshop (ITA)*, 2015, pp. 191–198.
- [9] H. Pirzadeh and A. L. Swindlehurst, "Spectral Efficiency of Mixed-ADC Massive MIMO," *IEEE Transactions on Signal Processing*, vol. 66, no. 13, pp. 3599–3613, 2018.
- [10] J. Zhang, L. Dai, Z. He, S. Jin, and X. Li, "Performance Analysis of Mixed-ADC Massive MIMO Systems Over Rician Fading Channels," *IEEE Journal on Selected Areas in Communications*, vol. 35, no. 6, pp. 1327–1338, 2017.
- [11] J. Chae and J. H. Cho, "An ADC-Aware Receiver Design for Multi-User MIMO Underlay System With Strong Cyclostationary Legacy Signal," *IEEE Access*, vol. 11, pp. 119788–119801, 2023.
- [12] C. Mollen, U. Gustavsson, T. Eriksson, and E. G. Larsson, "Spatial Characteristics of Distortion Radiated From Antenna Arrays With Transceiver Nonlinearities," *IEEE Transactions on Wireless Communications*, vol. 17, no. 10, pp. 6663–6679, 2018.
- [13] A. K. Saxena, I. Fijalkow, and A. L. Swindlehurst, "On one-bit quantized ZF precoding for the multiuser massive MIMO downlink," in *2016 IEEE Sensor Array and Multichannel Signal Processing Workshop (SAM)*, 2016, pp. 1–5.
- [14] O. B. Usman, H. Jedda, A. Mezghani, and J. A. Nossek, "MMSE precoder for massive MIMO using 1-bit quantization," in *2016 IEEE International Conference on Acoustics, Speech and Signal Processing (ICASSP)*, 2016, pp. 3381–3385.
- [15] S. Jacobsson, G. Durisi, M. Coldrey, T. Goldstein, and C. Studer, "Quantized Precoding for Massive MU-MIMO," *IEEE Transactions on Communication*, vol. 65, no. 11, pp. 4670–4684, Nov. 2017.
- [16] —, "Nonlinear 1-bit precoding for massive MU-MIMO with higher-order modulation," in *2016 50th Asilomar Conference on Signals, Systems and Computers*, 2016, pp. 763–767.
- [17] A. Mezghani, R. Ghiat, and J. A. Nossek, "Transmit processing with low resolution D/A-converters," in *2009 16th IEEE International Conference on Electronics, Circuits and Systems - (ICECS 2009)*, 2009, pp. 683–686.
- [18] J. Choi, J. Park, and N. Lee, "Energy Efficiency Maximization Precoding for Quantized Massive MIMO Systems," *IEEE Transactions on Wireless Communications*, vol. 21, no. 9, pp. 6803–6817, 2022.
- [19] E. Björnson, L. Sanguinetti, and J. Hoydis, "Hardware Distortion Correlation Has Negligible Impact on UL Massive MIMO Spectral Efficiency," *IEEE Transactions on Communication*, vol. 67, no. 2, pp. 1085–1098, 2019.
- [20] L. N. Ribeiro, S. Schwarz, M. Rupp, and A. L. F. de Almeida, "Energy Efficiency of mmWave Massive MIMO Precoding With Low-Resolution DACs," *IEEE Journal of Selected Topics in Signal Processing*, vol. 12, no. 2, pp. 298–312, 2018.
- [21] H. Huang, W. Xia, J. Xiong, J. Yang, G. Zheng, and X. Zhu, "Unsupervised Learning-Based Fast Beamforming Design for Downlink MIMO," *IEEE Access*, vol. 7, pp. 7599–7605, 2019.
- [22] W. Xia, G. Zheng, K.-K. Wong, and H. Zhu, "Model-Driven Beamforming Neural Networks," *IEEE Wireless Communications*, vol. 27, no. 1, pp. 68–75, 2020.
- [23] T. Feys, X. Mestre, E. Peschiera, and F. Rottenberg, "Deep Unfolding for Fast Linear Massive MIMO Precoders under a PA Consumption Model," in *2023 IEEE 97th Vehicular Technology Conference (VTC2023-Spring)*, 2023, pp. 1–5.
- [24] T. Feys, L. Van der Perre, and F. Rottenberg, "Toward Energy-Efficient Massive MIMO: Graph Neural Network Precoding for Mitigating Non-Linear PA Distortion," *IEEE Transactions on Cognitive Communications and Networking*, pp. 1–1, 2024.
- [25] T. Feys, X. Mestre, and F. Rottenberg, "Self-Supervised Learning of Linear Precoders under Non-Linear PA Distortion for Energy-Efficient Massive MIMO Systems," in *ICC 2023 - IEEE International Conference on Communications*, 2023.
- [26] P. W. Battaglia *et al.*, "Relational inductive biases, deep learning, and graph networks," 2018. [Online]. Available: <https://arxiv.org/abs/1806.01261>
- [27] I. Goodfellow, Y. Bengio, and A. Courville, *Deep Learning*. MIT Press, 2016, <http://www.deeplearningbook.org>.
- [28] B. Zhao, J. Guo, and C. Yang, "Understanding the performance of learning precoding policies with graph and convolutional neural networks," *IEEE Transactions on Communication*, vol. 72, no. 9, pp. 5657–5673, 2024.
- [29] —, "Learning Precoding Policy: CNN or GNN?" in *2022 IEEE Wireless Communications and Networking Conference (WCNC)*, 2022, pp. 1027–1032.
- [30] A. Balatsoukas-Stimming, O. Castañeda, S. Jacobsson, G. Durisi, and C. Studer, "Neural-Network Optimized 1-bit Precoding for Massive MU-MIMO," in *2019 IEEE 20th International Workshop on Signal Processing Advances in Wireless Communications (SPAWC)*, 2019, pp. 1–5.
- [31] O. Castañeda, S. Jacobsson, G. Durisi, M. Coldrey, T. Goldstein, and C. Studer, "1-bit Massive MU-MIMO Precoding in VLSI," *IEEE Journal on Emerging and Selected Topics in Circuits and Systems*, vol. 7, no. 4, pp. 508–522, 2017.
- [32] M. Hossienzadeh, H. Aghaeinia, and M. Kazemi, "Deep Learning Based Interference Exploitation in 1-Bit Massive MIMO Precoding," *IEEE Access*, vol. 11, pp. 17 096–17 103, 2023.
- [33] I. Bello, H. Pham, Q. V. Le, M. Norouzi, and S. Bengio, "Neural Combinatorial Optimization with Reinforcement Learning," 2017. [Online]. Available: <https://arxiv.org/abs/1611.09940>
- [34] A. I. Garmendia, J. Ceberio, and A. Mendiburu, "Neural Combinatorial Optimization: a New Player in the Field," 2022. [Online]. Available: <https://arxiv.org/abs/2205.01356>
- [35] Y. Bengio, A. Lodi, and A. Prouvost, "Machine learning for combinatorial optimization: A methodological tour d'horizon," *European Journal of Operational Research*, vol. 290, no. 2, pp. 405–421, 2021.
- [36] R. Wang, L. Shen, Y. Chen, X. Yang, D. Tao, and J. Yan, "Towards One-shot Neural Combinatorial Solvers: Theoretical and Empirical Notes on the Cardinality-Constrained Case," in *The Eleventh International Conference on Learning Representations*, 2023.
- [37] I. A. M. Huijben, W. Kool, M. B. Paulus, and R. J. G. van Sloun, "A Review of the Gumbel-max Trick and its Extensions for Discrete Stochasticity in Machine Learning," *IEEE Transactions on Pattern Analysis and Machine Intelligence*, vol. 45, no. 2, pp. 1353–1371, 2023.
- [38] A. K. Fletcher, S. Rangan, V. K. Goyal, and K. Ramchandran, "Robust Predictive Quantization: Analysis and Design Via Convex Optimization," *IEEE Journal of Selected Topics in Signal Processing*, vol. 1, no. 4, pp. 618–632, 2007.

- [39] O. T. Demir and E. Bjornson, “The Bussgang Decomposition of Non-linear Systems: Basic Theory and MIMO Extensions [Lecture Notes],” *IEEE Signal Processing Magazine*, vol. 38, no. 1, pp. 131–136, 2021.
- [40] A. Gersho and R. Gray, *Vector Quantization and Signal Compression*, ser. The Springer International Series in Engineering and Computer Science. Springer US, 1991.
- [41] T. Hwang, C. Yang, G. Wu, S. Li, and G. Ye Li, “OFDM and Its Wireless Applications: A Survey,” *IEEE Transactions on Vehicular Technology*, vol. 58, no. 4, pp. 1673–1694, 2009.
- [42] J. Max, “Quantizing for minimum distortion,” *IRE Transactions on Information Theory*, vol. 6, no. 1, pp. 7–12, 1960.
- [43] D. P. Kingma and J. Ba, “Adam: A Method for Stochastic Optimization,” 2014. [Online]. Available: <https://arxiv.org/abs/1412.6980>
- [44] E. Jang, S. Gu, and B. Poole, “Categorical Reparameterization with Gumbel-Softmax,” 2017.
- [45] K. Hornik, M. Stinchcombe, and H. White, “Multilayer feedforward networks are universal approximators,” *Neural networks*, vol. 2, no. 5, pp. 359–366, 1989.
- [46] W. L. Hamilton, “Graph Representation Learning,” *Synthesis Lectures on Artificial Intelligence and Machine Learning*, vol. 14, no. 3, pp. 1–159.
- [47] K. Guo, W. Li, Z. Zhu, S. Zeng, T. Xie, S. HA, Y. Xie, P. Debacker, M. Verhelst, and Y. Wang, “Neural network accelerator comparison.” [Online]. Available: <https://nicsefc.ee.tsinghua.edu.cn/networkone.html>
- [48] Z.-S. Fu, Y.-C. Lee, A. Park, and C.-H. Yang, “A 40-nm 646.6tops/w sparsity-scaling dnn processor for on-device training,” in *2022 IEEE Symposium on VLSI Technology and Circuits (VLSI Technology and Circuits)*, 2022, pp. 40–41.
- [49] T. Miao, T. Feys, G. Callebaut, J. V. Mulders, E. Peschiera, M. A. Rahman, and F. Rottenberg, “GNN-based Precoder Design and Fine-tuning for Cell-free Massive MIMO with Real-world CSI,” 2025. [Online]. Available: <https://arxiv.org/abs/2505.08788>
- [50] L. Wang, X. Zhang, H. Su, and J. Zhu, “A comprehensive survey of continual learning: Theory, method and application,” 2024. [Online]. Available: <https://arxiv.org/abs/2302.00487>
- [51] Juan Montojo. Overview of AI/ML related work in 3GPP. ETSI AI Conference 2025. [Online]. Available: [https://docbox.etsi.org/Workshop/2025/02\\_AICONFERENCE/SESSION05/3GPPRAN\\_MONTOJO\\_JUAN\\_QUALCOMM.pdf](https://docbox.etsi.org/Workshop/2025/02_AICONFERENCE/SESSION05/3GPPRAN_MONTOJO_JUAN_QUALCOMM.pdf)